Multiabsorber transition-edge sensors for x-ray astronomy

Stephen J. Smith
Joseph S. Adams
Simon R. Bandler
James A. Chervenak
Aaron M. Datesman
Megan E. Eckart
Fred M. Finkbeiner
Ruslan Hummatov
Richard L. Kelley
Caroline A. Kilbourne
Antoine R. Miniussi
Frederick S. Porter
John E. Sadleir
Kazuhiro Sakai
Nicholas A. Wakeham
Edward J. Wassell

SPIE.

Multiabsorber transition-edge sensors for x-ray astronomy

Stephen J. Smith,[a,b,][*] Joseph S. Adams,[a,b] Simon R. Bandler,[a] James A. Chervenak,[a] Aaron M. Datesman,[a,c]
Megan E. Eckart,[a] Fred M. Finkbeiner,[a,d] Ruslan Hummatov,[a,b] Richard L. Kelley,[a] Caroline A. Kilbourne,[a]
Antoine R. Miniussi,[a,b] Frederick S. Porter,[a] John E. Sadleir,[a] Kazuhiro Sakai,[a,b] Nicholas A. Wakeham,[a,b] and
Edward J. Wassell[a,c]

[a]NASA Goddard Space Flight Center, Greenbelt, Maryland, United States
[b]University of Maryland Baltimore County, Center for Research and Exploration in Space Science and Technology, Maryland, United States
[c]Science Systems and Applications Inc., Lanham, Maryland, United States
[d]Sigma Space Corporation, Lanham, Maryland, United States

Abstract. We are developing arrays of position-sensitive microcalorimeters for future x-ray astronomy applications. These position-sensitive devices commonly referred to as hydras consist of multiple x-ray absorbers, each with a different thermal coupling to a single-transition-edge sensor microcalorimeter. Their development is motivated by a desire to achieve very large pixel arrays with some modest compromise in performance. We report on the design, optimization, and first results from devices with small pitch pixels (<75 μm) being developed for a high-angular and energy resolution imaging spectrometer for Lynx. The Lynx x-ray space telescope is a flagship mission concept under study for the National Academy of Science 2020 decadal survey. Broadband full-width-half-maximum (FWHM) resolution measurements on a 9-pixel hydra have demonstrated $\Delta E_{FWHM} = 2.23 \pm 0.14$ eV at Al-K$_\alpha$, $\Delta E_{FWHM} = 2.44 \pm 0.29$ eV at Mn-K$_\alpha$, and $\Delta E_{FWHM} = 3.39 \pm 0.23$ eV at Cu-K$_\alpha$. Position discrimination is demonstrated to energies below <1 keV and the device performance is well-described by a finite-element model. Results from a prototype 20-pixel hydra with absorbers on a 50-μm pitch have shown $\Delta E_{FWHM} = 3.38 \pm 0.20$ eV at Cr-K$_{\alpha 1}$. We are now optimizing designs specifically for Lynx and extending the number of absorbers up to 25/hydra. Numerical simulation suggests optimized designs could achieve ~3 eV while being compatible with the bandwidth requirements of the state-of-the art multiplexed readout schemes, thus making a 100,000 pixel microcalorimeter instrument a realistic goal. © The Authors. Published by SPIE under a Creative Commons Attribution 4.0 Unported License. Distribution or reproduction of this work in whole or in part requires full attribution of the original publication, including its DOI. [DOI: 10.1117/1.JATIS.5.2.021008]

Keywords: position-sensitive detector; hydra; microcalorimeter; transition-edge sensor; Lynx; imaging array.

Paper 18097SS received Nov. 1, 2018; accepted for publication Mar. 18, 2019; published online Apr. 8, 2019.

1 Introduction

Transition-edge sensors (TESs) are sensitive microcalorimeters under the development for a variety of applications in photon and particle spectroscopy.[1,2] These devices consist of a thin superconducting film that is electrically biased in the highly temperature sensitive superconducting-to-normal transition region. Absorption of photon or particle energy causes a change in resistance of the sensor, which is measured as a current change by a superconducting quantum interference device (SQUID) ammeter. We are currently pursuing large format TES arrays[3,4] to meet the requirements of proposed future x-ray astronomy missions.[5,6] These applications require high fill-factor, kilo-pixel arrays capable of achieving full-width-half maximum (FWHM) energy resolution, ΔE_{FWHM}, of typically a few electron volts in the energy range 0.3 to 10 keV. The maximum number of pixels used in TES arrays is constrained by a number of practical challenges. Position-sensitive microcalorimeters are an alternative approach that provides a means to increase the number of pixels within an array, at some compromise in performance, without the commensurate increase in the number of readout components, wires, and electrical connections. Although position-sensitive microcalorimeters have been investigated in a variety of different

forms,[7–11] our recent focus has been on the use of multiabsorber TESs commonly referred to as "hydras."[12,13] These devices consist of a series of individual x-ray absorbers with a different thermal conductance or "link" to a single TES. Each of these links acts as a thermal low-pass filter that gives rise to a different characteristic pulse shape for an x-ray absorbed in each pixel of the hydra. Thus these detectors can be used to provide larger focal plane coverage, or improved angular resolution for the same coverage, at some expense of performance (energy resolution and counting-rate) when compared to arrays of independent pixels. This type of detector has been proposed for a variety of different x-ray mission concepts over the past decade such as the international x-ray observatory (IXO).[11,12] For IXO, the hydras were proposed as a way to increase the size of the focal-plane array around a core main array of single-pixel TESs and thus provide a greatly expanded instrument field-of-view (FOV) with only a limited increase in complexity. Results from prototype 4-pixel hydras have demonstrated $\Delta E_{FWHM} = 5$ to 6 eV at an x-ray energy of 5.9 keV for devices with a 0.25-mm absorber pitch.[12,13]

Our recent focus of hydras has pivoted toward high-angular resolution solar physics and x-ray astronomy applications incorporating a greater number of small pixels (<75 μm) per TES. Lynx is a large mission concept currently under study for the National Academy of Sciences (NAS) 2020 decadal survey.[6] The proposed Lynx design combines a subarcsecond x-ray optic with a microcalorimeter imaging spectrometer

---

incorporating ~100,000 pixels. The microcalorimeter instrument will provide nondispersive spectroscopy with $\Delta E_{\text{FWHM}} \sim$ 3 eV in 1" pixels over the energy band 0.2 to 7 keV. The only way to realize these very large format pixel arrays using microcalorimeters is by utilizing multipixel hydras. The Lynx x-ray microcalorimter (LXM) array design is still in formulation but as presently envisaged assumes a main array with a 5' FOV that consists of 1" (50 μm) pixels arranged in hydras consisting of up to 25 pixels/hydra. Additional enhancement subarrays such as a 1' FOV 25-pixel hydra array with 0.5" (25 μm) pixels, and a single-pixel array of 1" pixels optimized for energies below 1 keV, are also under consideration.

Single-pixel TESs of pitch 250 μm, being designed for missions such as ESA's Athena, routinely achieve resolution of ~2 eV at 6 keV. Our proposed hydra designs for Lynx use the same 250-μm pitch per TES but with up to 25 separate pixels as opposed to one large pixel, which in combination with the high-resolution optic, provided greater angular sensitivity with only a modest comprise in resolution. Thus by combining the spectroscopy capabilities of ESA's planned Athena mission[5] with the angular resolution of NASA's Chandra mission,[14] Lynx will revolutionize x-ray astronomy by providing answers to key science themes related to galaxy formation and evolution as well as the energetics of stellar evolution.

In this paper, we report on the first small pixel hydras that are being developed for applications such as Lynx. In Sec. 2, we start by outlining the basic theory behind multiabsorber microcalorimeters and describe the modeling used to design the hydra and predict its performance. The design and performance of the first miniature 4-pixel and 9-pixel hydras are discussed in Sec. 3. In Sec. 4, we report on the design and preliminary results from a single hydra with 20 pixels, which is a precursor to new devices (discussed in Sec. 5) that will be optimized specifically for LXM array.

2 Multipixel TES Theory and Modeling

The detailed theory for position-sensitive microcalorimeter detectors has been presented elsewhere[7,15,16] and here we summarize the relevant points for this particular design. A TES microcalorimter consists of a superconducting thin-film sensor that is thermally connected to an x-ray absorber. Assuming only the electrical Johnson noise of the TES and thermal fluctuation noise between the TES and heat bath, the energy resolution ΔE_{FWHM} is well-described by[1]

$$\Delta E_{\text{FWHM}} \approx 2.355 \sqrt{4k_b T^2 \frac{C}{\alpha} \sqrt{\frac{nF(T, T_b, n)(1 + 2\beta)}{1 - (T_b/T_0)^n}}}, \quad (1)$$

where C is the total device heat capacity (typically dominated by the absorber), T is the TES temperature, T_b is temperature of the heat bath, k_b is Boltzmann's constant, n and F are the unit-less constants that depend upon the physical nature of the thermal link to the heat bath. α ($= T/R\partial R/\partial T$) and β ($= I/R\partial R/\partial I$) are unit-less constants that are used to parameterize the local slope of the TES resistive transition surface $R(T, I)$ at the operating point. The principle behind the hydra is to segment a single large absorber into a series of smaller absorbers. Each of these absorbers acts as a separate imaging element or pixel. Each absorber has a thermal link to the TES that decouples the absorbers from the sensor and slows the transmission of heat to the TES. The thermal conductance of each link is tuned
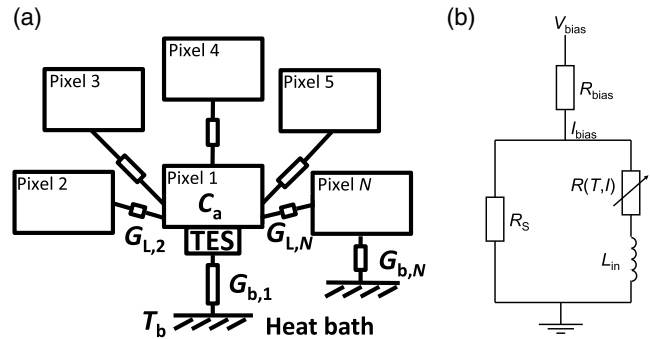

Fig. 1 (a) Thermal model of a multiabsorber TES consisting of N x-ray absorbers of heat capacity C_a, connected to a single TES via a conductance G_{Li}. The TES and absorbers are weakly thermally coupled to a heat bath of temperature T_b via conductance G_{bi} (for clarity G_{bi} is only shown for pixel 1 and pixel N). (b) Electrical bias circuit for the TES of resistance $R(T, I)$.

so that the TES measures a different characteristic temperature profile for x-ray hits in the different absorbers, before all absorbers come into thermal equilibrium with each other. It is the initial pre-equilibration part of the measured pulse that is used to determine the event position. The electrothermal model for the hydra is depicted in Fig. 1. Hydras have an intrinsic trade-off between energy resolution and position sensitivity that depends upon the ratio of the internal thermal conductances between absorbers, to the external thermal conductance to the bath. If the pixels are too well thermally coupled together, such that hydra comes into thermal equilibrium over time scales much shorter than decay time constant to the heat bath, the device will essentially act as one macropixel with ΔE_{FWHM} described by Eq. (1) and, consequently, no position discrimination between its subpixels. Reducing the internal conductances relative to the bath conductance introduces position dependence but the low-pass filtering of the pulse shape attenuates the signal relative to the detector noise. Since each link is tuned to a different conductance value, ΔE_{FWHM} is expected to be different for each pixel and will be slightly degraded from the single-pixel limit of Eq. (1). Since the position sensitivity also depends on the signal-to-noise ratio, if the conductances are too small the position resolution will also become degraded. Consequently, there is a required design optimization of the link conductances to maximize the signal-to-noise while maintaining enough separation between pulse shapes to determine position. The decoupling of the absorbers also adds internal thermal fluctuation noise between each absorber and the TES, however, for optimized designs this is usually not a significant contribution.

In a microcalorimeter, the energy of an absorbed photon E is determined using a precomputed digital optimal filter.[17] The optimal filter is generated from knowledge of the detector responsivity to x-rays and the noise properties of the device. The hydra detector is no different except because there are multiple pixels and therefore pulse shapes, a filter must be determined for each individual pixel. In order to apply the correct filter for energy estimation, the correct pixel position and thus template must be first determined. We are studying various approaches to determine event position. By far, the simplest and preferred approach is to use a single rise-time estimate of the measured pulse. However, we are also exploring alternative approaches that may offer improved position sensitivity such as χ^2 minimization between the measured pulse and precomputed template pulse.[18] This uses more of the pre-equilibration

pulse shape than a simple two-point rise-time determination and thus may offer improved performance in low signal-to-noise cases, where a simple rise-time estimator may not be adequate. We have also developed a correlated-energy-position-optimal-filter algorithm.[16] This approach uses an iterative convergence algorithm to simultaneously calculate the energy and position of the event without *a priori* assumptions about either. The implementation is technically challenging and for simplicity in our present analysis we do not use this algorithm for signal processing analysis of real data but as a design tool for optimizing the link values and predicting the fundamental limits on resolution. In the hydra, the ability to distinguish between different pulses depends on the photon energy E. Below some energy E_0, the signal-to-noise ratio will be sufficiently degraded such that it is not possible to adequately distinguish between events in different pixels and the position resolution will start to degrade. Initially, this will be limited to the absorbers with most similar pulse shape characteristics but at low enough energies, the error in the position assignment may be spread across many pixels. When this occurs, E and x are correlated such that incorrect position assignment will result in an additional broadening to ΔE_{FWHM}, thus it is desirable to design the detector such that E_0 is sufficiently below the lower limit of the energy bandpass required for the given application. For most astrophysics applications, this is typically a few hundred electron volts.

In order to model and design the hydra, we use the finite-element model and numerical algorithms discussed in Ref. 16. The electrothermal models depicted in Fig. 1 consists of a series of N x-ray absorbers, each with heat capacity C_a, connected to a single TES via a thermal conductance G_{Li} (where i is the pixel number from 1 to N). The TES and absorbers are weakly thermally coupled to a heat bath of temperature T_b via conductance G_{bi}. The TES is electrically voltage biased using a shunt resistor R_s in parallel with the TES and is magnetically coupled to an SQUID read-out and electronics chain via an input coil with inductance L_{in}. The first pixel is assumed infinitely thermally coupled to the TES so is considered as a single-lumped element in our models. The coupled nonlinear differential equations that describe a general N pixel hydra can then be written as

$$L_{\mathrm{in}}\dot{I} = V_0 - I[R_L + R(T, I)], \tag{2}$$

$$C_a\dot{T}_1 = P_{\mathrm{Joule}} - P_{b1} - \sum_{i=2}^{i=N} P_{Li}, \tag{3}$$

$$C_a\dot{T}_i = -P_{bi} + P_{L_i}, \tag{4}$$

where we assume the TES resistance has linear current- and temperature-dependent transition of the form

$$R(T, I) = R_0 + \frac{dR}{dT}(T - T_0) + \frac{dR}{dI}(I - I_0). \tag{5}$$

R_0, T_0, and I_0 are the detector resistance, temperature, and current at the quiescent operating point, respectively, and dR/dT and dR/dI are the local slopes of the temperature and current dependence of the transition, respectively. Equation (2) is the electrical circuit equation that describes the time evolution of the TES current, where V_0 is the Thevenin equivalent bias voltage and R_L is the bias load resistor [$R_L = (1/R_S + 1/R_{\mathrm{bias}})^{-1} \equiv R_s$]. Equation (3) describes the temperature evolution T_1 of the first pixel directly coupled to the TES.

$P_{\mathrm{joule}} = I^2R(T, I)$ is the power dissipation in the sensor that maintains the TES in its transition. The power flow between the first pixel and the heat bath at temperature T_b is described by $P_{b1} = k_{b1}(T_1^n - T_b^n)$. This first pixel is then thermally connected to the all other pixels in the hydra by a thermal conductance G_{Li}. The resulting power flow between these other pixels and the first pixel P_{Li} follows the same functional form as P_{bi}; the exact values of the conductivity k and exponent n depend on the physical properties of the thermal links between the elements. The remaining pixels that are connected to pixel 1 are described by equations of the same form as Eq. (4). Following the procedures described in Ref. 16, we can numerically integrate these coupled nonlinear differential equations to solve for the time evolution $I(t)$ and $T_i(t)$ resulting from x-ray absorption in any pixel element. By linearizing for small changes in ΔT and ΔI and taking the Fourier transform, we can also calculate the total detector noise power spectral density as well as the predicted energy resolution. This analysis includes additional inputs to Eqs. (2)–(4) that describe the power spectral densities for the TES and load resistor electrical Johnson noise, the thermal noise between the each pixel and the heat bath, as well as the internal thermal fluctuation noise associated with the link between each pixel.

3 Small Pitch Hydra Design

3.1 *Detector Design and Basic Properties*

We have designed and fabricated test wafers that include close-packed arrays of single pixels (with only 1 absorber), 4-pixel, 9-pixel, and 20-pixel hydras. The design and performance of the single-pixel devices have been reported elsewhere.[19] Here we focus primarily on the 9-pixel designs but also briefly comment on the 4-pixel performance. The 20-pixel designs are discussed in Sec. 4.

Figure 2 shows a schematic diagram and scanning electron microscope (SEM) image of the 9-pixel hydra. We use a Mo (60 nm)/Au(185 nm) bilayer TES of lateral dimensions $30 \times 35~\mu\mathrm{m}^2$. The TES design is identical for the single, 4-, and 9-pixel hydras. Unlike previous 4-pixel hydra designs, these small pitch versions lack the membrane defining back-etch and are fabricated directly on a Si wafer that utilizes a $\sim 1~\mu\mathrm{m}$-thick Cu heat sink layer for thermal cross-talk mitigation.[20] The x-ray absorbers are electroplated Au with lateral dimensions $65 \times 65~\mu\mathrm{m}^2$ and are 5.2-$\mu\mathrm{m}$ thick. This provides a stopping power of 98% at an energy of $E = 6$ keV. The absorbers are cantilevered $\sim 4.0~\mu\mathrm{m}$ above the TES and substrate, supported by pillar-shaped stems. The contact area of each support stem with the TES or the substrate is $3.5 \times 3.5~\mu\mathrm{m}^2$ (<1% of the absorber area) and is minimized compared to previous designs in order to reduce the loss of energetic athermal phonons directly to the substrate that has been shown to result in a non-Gaussian broadening of ΔE_{FWHM}.[21] The absorber directly above the TES has five support stems, whereas all other absorbers have three. The absorber above the TES makes direct contact to the sensor via a stem in the center of the TES (ensuring there is a strong thermal connection between the sensor and the absorber). The other eight absorbers connect to the TES via Au sputtered links (of thickness $d = 482 \pm 2$ nm). The links connect the absorbers via their support stems, thus they do not make direct contact to the TES but are thermally connected through its absorber. The thermal conductance through the absorber is much greater than that of the
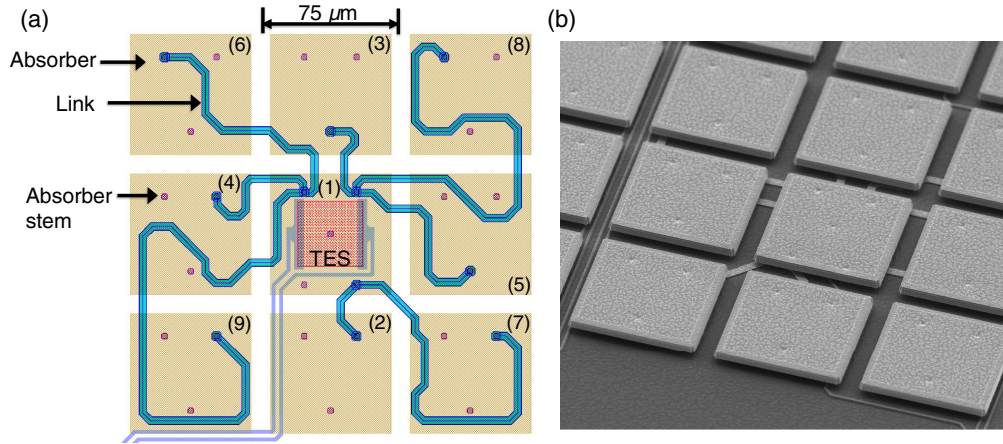
Fig. 2 (a) Schematic layout of a 9-pixel hydra and (b) SEM image of a 9-pixel hydra. Visible between the gaps in the absorbers are the thermal links that connect the TES to each pixel.

links so it does not affect the total conductance between absorbers. The resistivity ρ of the link material at $T = 4.2$ K is measured to be $\rho = 0.49 \pm 0.01\ \mu\Omega\,$cm. The devices are fabricated in 8×8 close-packed arrays where each 9-pixel hydra is on a 225-μm pitch and the 4-pixel design is on a 150-μm pitch. The heat capacity of each absorber, $C_a \approx 0.177$ pJ/K (referenced at 100 mK), was measured for a single-pixel device and is dominated by the thick Au absorber. The total heat capacity is then ≈ 1.6 pJ/K for the 9-pixel hydra and ≈ 0.7 pJ/K for the 4-pixel hydra. The links and TES are calculated to contribute only $\sim 1\%$ to the total detector heat capacity. These TESs have a measured normal state resistance of $R_n \approx 20$ mΩ and are voltage biased in the transition using a ~ 0.2-mΩ microfabricated Pd/Au shunt resistor in the parallel with the TES. The transition temperature, $T_C = 79 \pm 1$ mK, was measured on 10, 9-pixel hydras using a small excitation current ($I \sim 1\ \mu$A). However, due to the lateral proximitisation effect from the electric bias leads, the transition temperature is highly current dependent[22] and temperature of the device under bias is estimated to be $T_0 \approx 46$ mK (where $I \approx 52\ \mu$A).

The thermal conductance of a link of length L, and width w, at temperature T can be calculated from the Wiedemann–Franz relation[23]

$$G_{Li} = 24.5T\frac{d}{\rho}\frac{w}{L}\ \text{(nW/K)}. \tag{6}$$

In order to design the required length of each thermal link within the footprint of a single hydra and without compromising the fabrication yield, a series of 45-deg bends are incorporated into the design. The designs reported here have 4-μm-wide links. In Table 1, we summarize the length and the calculated thermal conductance for each link. Each link not only couples the absorbers to the sensor but also provides a parallel path for power to flow to the heat bath. Ideally, the total thermal conductance from the links to the bath would be significantly less than the contribution from the TES; this would allow independent optimization of the internal thermal time constants without simultaneously affecting the time constant to the bath. However, practical constraints on the design of the links mean that this is typically not possible. There are two possible mechanisms that may contribute to the thermal conductance between thin metal films and dielectric substrates.[24] *A priori*,

it was not clear which would be the dominant mechanism. A Kapitza boundary conductance G_{kap} arises because of an acoustic mismatch between the phonons in the film and a substrate, which will scale with the interface area A, $G_{\text{kap}} = 4\sigma AT^3$ ($\sigma = 158$ W m^{-2} K^{-4} for bulk Au on Si[25]). For acoustic mismatch theory to be valid, the film thickness d must be large enough to support an independent phonon population. This leads to a requirement that the phonon wavelength is at least as short as d, $\hbar\nu_s/2k_bT < d$, where ν_s is the speed of sound. Estimating $\langle\nu_s\rangle \sim 3000$ m/s at 50 mK averaged over all phonon modes, we require $d > 220$ nm. This is comparable to the film thickness of our TES (245 nm) but approximately half that of the links (482 nm). In addition to the Kapitza conductance an electron–phonon (e–ph) decoupling term may also exist, the e–ph conductance will scale with the volume of electrons V in the metal film available to couple to the phonons $G_{\text{e–ph}} = 5\Sigma VT^4$ (the e–ph coupling parameters for metals such as gold are typically around $\Sigma \approx 2 \times 10^9$ W m^{-3} K^{-5}.) Whichever term dominates will depend upon the geometry and temperature of the film.

From measurements of the bias power in the transition as a function of T_b, $P = k(T^n - T_b^n)$ and fitting for the parameters k, T, and n, we can calculate the differential thermal conductance to the heat sink $G_b \equiv dP/dT = nkT^{n-1}$. We find the total conductance $G_b = 372 \pm 20$ pW/K at T_0. From characterization of single-pixel devices[19] from the same wafer as these hydras, we estimate the contribution for the TES to the bath alone is $G_b = 31 \pm 5$ pW/K (we note this is comparable to the estimated value for e–ph, but 3 times less than that estimated for the Kapitza conductance for bulk Au on Si). Thus the total conductance to the bath is dominated by the links. The ratio of the link contribution to the total conductance to that of the TES alone is ~ 11. However, the ratio of the link area to that of the TES is only ~ 3.8 and the equivalent volumetric ratio is 7.5. Therefore, the increased thermal conductance from the links to the bath is larger than can be accounted for by either the increased area or increased volume alone. This implies that neither a single Kapitza boundary conductivity, nor a single e–ph coupling parameter, can simply be used to describe both the TES and the link conductances to the bath.

It is likely that the thicker films of the links compared to that of the TES are the reason for the enhanced per area, or per volume, conductance from the links. However, more data are now

Table 1 Summary of the length and calculated thermal conductance of each link for a 9-pixel hydra. Pixel 1 is directly connected to the TES via its absorber so has no link. Also shown is the calculated contribution that the TES (pixel 1) and each link contribute to the total thermal conductance to the heat bath.

Pixel, i	Link length (μm)	G_{Li} (nW/K)	G_{bi} (pW/K)
1	n/a	n/a	31.2
2	33	13.55	9.6
3	46	9.72	13.3
4	70	6.39	20.4
5	96	4.66	27.9
6	135	3.31	39.3
7	196	2.28	57.0
8	258	1.73	75.0
9	338	1.32	98.3

required for devices of different link thicknesses and on different substrates to better understand the role of Kapitza and e–ph coupling in these devices.

The thermal path may be further complicated because of the buried heat-sink layer incorporated into these designs. These devices are not fabricated directly on top of thick Si but rather on a multilayer stack comprised of a SiO$_2$ (330 nm) followed by the thick heat-sinking layer of W(50 nm)/Cu(3 μm)/W(50 nm). Thus there is likely also a boundary resistance between the thin SiO$_2$ layer and the heat sink layers. The effect of this layer has not been studied but will also be the subject of future investigations.

Table 1 summarizes the estimated thermal conductance from the TES and links to the heat bath. The sum of which equals the total measured conductance. We note that in order to appropriately represent the conductance to the heat bath associated with each link, in our lumped finite-element-model (which in reality is distributed across the full length of the link), we split half of each value listed in Table 1 between the 2 pixels being connected by the relevant link. For example, the conductance between pixel 1 and the bath includes the TES-to-bath conductance plus half of all links to bath conductances.

3.2 X-Ray Response and Energy Resolution

The bath temperature was controlled to $T_b = 40$ mK and devices were operated in the transition at a quiescent bias point of 3% R_n, where the best signal-to-noise performance was achieved. Measured x-ray events are designated to a pixel according to their rise time τ_{rise}. The rise time is determined from the 20% to 80% points of the peak in the pulse height. Once the pixel has been identified, the energy is calculated from a single-digital optimal filter referenced to each pixel.

Figure 3 shows the measured change in current $-\Delta I$ that occurs from photon absorption in each of the 9 pixels of the hydra. Each trace is the average of ~500 Mn-K$_\alpha$ x-ray events. The pulse shape with the fastest rise time and largest pulse height corresponds to the pixel directly thermally coupled to

the TES. For this pixel, the rise time is only limited by the electrical bandwidth of the readout circuit. The pulse rise time becomes slower and the pulse height smaller as the thermal conductance of each link is reduced. After the initial position-dependent signal (~125 μs), the pulses decay to the equilibrium bias point with the same exponential time constant of 1.3 ms.

Shown in Fig. 3(b) are the simulated pulse shapes using the parameters described in the previous section. The small signal transition parameters (α and β) required for modeling the pulse shapes have not been directly measured for these devices. However, to provide qualitative comparison to the measured pulse shapes, we use estimates of the transition parameters from other devices of similar size and geometry.[21,26] We choose $\alpha = 100$, $\beta = 10$, and the resulting pulse shapes gives good qualitative agreement with the measured data.

Figure 4 shows the rise time versus peak pulse height for x-ray events generated from an Mg (1.25 keV) and Al (1.49 keV) secondary fluorescence source. Events corresponding to the Al-K$_\alpha$ complex for each pixel are indicated. The population of events with lower pulse height (with the same τ_{rise} as the Al-K$_\alpha$ events) corresponds to Mg-K$_\alpha$ events. Figure 4(b) shows an expanded view of the same data showing only the first 5 pixels.

We can evaluate the position sensitivity from the ratio of the separation between the mean of the rise-time distributions for each pixel $\delta\mu$ to the width of each distribution σ. The mean μ and standard deviation σ of each rise-time distribution are determined by fitting a Gaussian to the histogram of rise-time populations associated with each pixel, including only Al-Kα events. We find that $\delta\mu/\sigma$ is around 25 for pixels 1 to 5 and 45 for pixels 6 to 9. Thus, the position sensitivity varies by less than a factor of two across the pixels and pixels are easily distinguishable from each other at these energies. Minor adjustments to the link conductances in future design iterations will be made to make the position sensitivity even more uniform. Since the position sensitivity scales with the inverse of the energy ($\Delta x \propto 1/E$),[15] we can estimate at what energy the rise-time distributions might start to overlap and result in position uncertainty between nearest neighbor distributions. We estimate that $\delta\mu/\sigma \geq 4$ for all pixels down to a photon energy of ~225 eV. Even at $\delta\mu/\sigma = 4$, only ~5% of events in a given pixels rise-time distribution would overlap with its nearest neighbor and result in position uncertainty for those events. Significant uncertainty between nearest neighbors will occur only when $\delta\mu \approx \sigma$, which is predicted to occur at energies below ~75 eV. Thus these devices have excellent position discrimination over a broad range of energies.

Once the pixels have been identified, the photon energy is measured using a digital optimal filter derived from the average pulse shape for each pixel. Digital optimal filtering is valid under the assumption that the noise properties are stationary and the detector response is linear. However, the voltage bias circuit used for TES operation results in a measured current response that is inherently nonlinear with photon energy and noise properties that are nonstationary during the pulse. Thus we apply a linearization transform to the measured data before the digital optimal filter is calculated and applied. We have previously shown that under certain conditions this can linearize the pulse response with energy and make the noise properties more stationary during a pulse. This in turn can improve the resolution.[26]
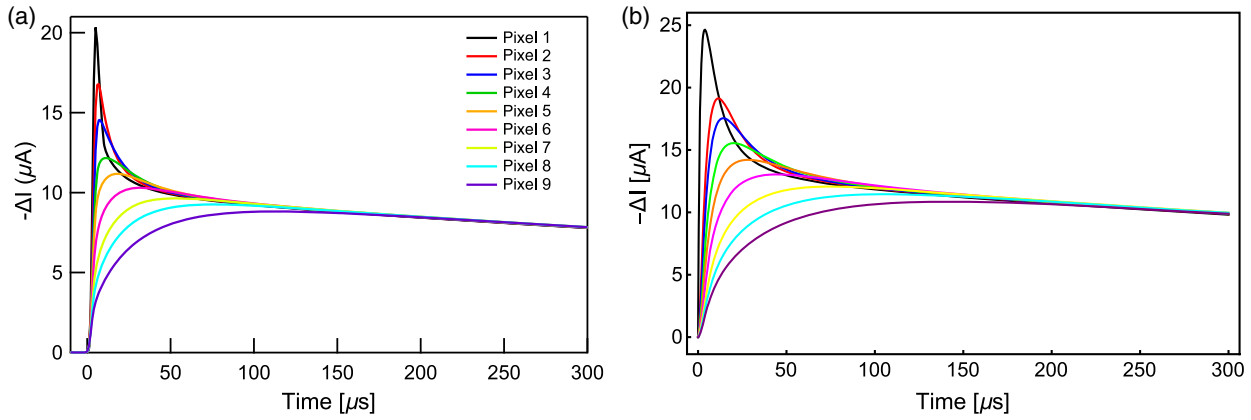
Fig. 3 (a) Measured average current pulses for 5.9 keV x-rays absorbed in each pixel of a 9-pixel hydra. Only the first 300 μs of the pulses are shown. After the initial position-dependent pre-equilibration signal, the pulses decay with the same exponential time constant of 1.3 ms. The pulse shape with the fastest rise-time corresponds to pixel 1 and the pulse with the slowest rise-time is pixel 9. (b) The simulated pulse shapes calculated using the modeling and parameters discussed in the main text. The pulse shapes show good qualitative agreements with the measured data.
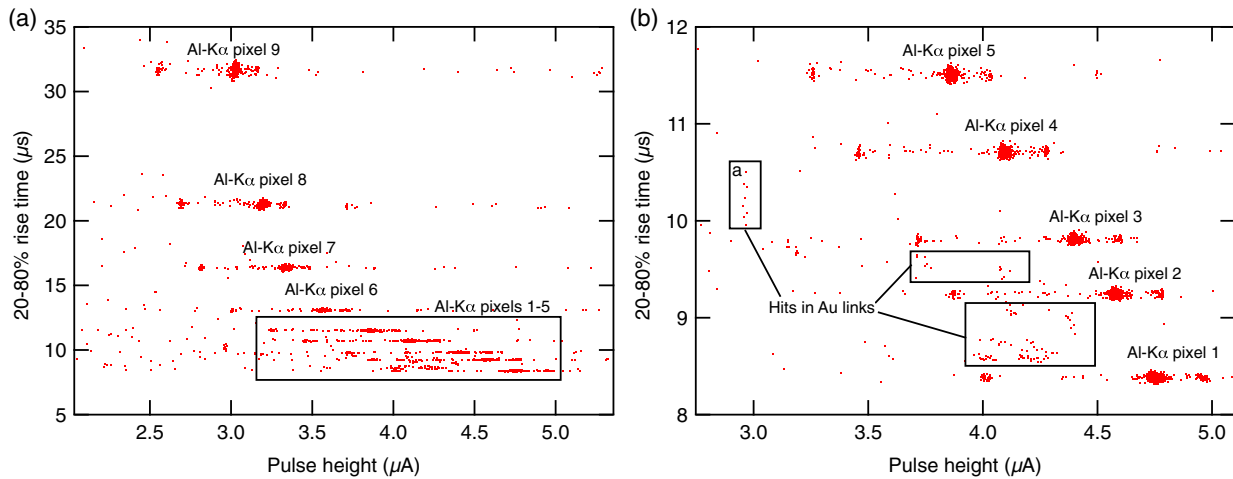

Fig. 4 (a) Measured rise time versus pulse height for a 9-pixel hydra for Mg (1.25 keV) and Al (1.49 keV) x-rays. (b) Zoom-in of the boxed region shown in (a) showing pixels 1 to 5 only. Using this simple rise-time algorithm, the event position is easily determined to energies of ≤ 1 keV. The boxed regions in (b) are attributed to events absorbed in the exposed links and account for <1% of the total measured events. The average of the group of events in the boxed region labeled "a" is shown in Fig. 6.

Figures 5(a)–5(c) show the co-added spectra including all 9 pixels in a single hydra for photon energies of $E = 1.5$ keV (Al-K$_\alpha$), 5.9 keV (Mn-K$_\alpha$), and 8 keV (Cu-K$_\alpha$), respectively. Data were taken on three separate acquisition runs with the same operating conditions. The quadrature averages, or root mean square (RMS), of the fitted energy resolutions of all 9 pixels are $\Delta E_{FWHM} = 2.23 \pm 0.14$ eV at Al-K$_\alpha$, $\Delta E_{FWHM} = 2.44 \pm 0.29$ eV at Mn-K$_\alpha$, and $\Delta E_{FWHM} = 3.39 \pm 0.23$ eV at Cu-K$_\alpha$. These are consistent with the fitted resolution of the co-added spectra. Also shown [Fig. 5(d)] are the individual fits for just the Mn-K$_\alpha$ measurement illustrating the high level of ΔE_{FWHM} uniformity within the hydra. Using the device design parameters and numerical simulations discussed in Secs. 2 and 3.1, we calculate that the combined 9-pixel hydra energy resolution is only degraded by ~10% compared to that expected for a single-pixel device with the same device properties and total heat capacity. Thus the introduction of position discrimination in these devices does not come at a significant penalty in energy resolution and the internal thermal links

are well optimized. Although high statistics broadband spectral measurements have not been studied on many hydras, lower statistic measurements on 10 hydras in a single array, have demonstrated good consistency in the rise times. This suggests that the device yield and uniformity properties are generally good.

The 4-pixel design demonstrated $\Delta E_{FWHM} = 1.44 \pm 0.09$ eV at Al-K$_\alpha$ and $\Delta E_{FWHM} = 2.08 \pm 0.08$ eV Mn-K$_\alpha$. For comparison, measurements on single-pixel devices from the same fabricated wafer have demonstrated resolution as good as $\Delta E_{FWHM} = 0.87 \pm 0.03$ eV at Al-K$_\alpha$ and $\Delta E_{FWHM} = 1.56 \pm 0.13$ eV at Mn-K$_\alpha$.[19] The energy resolution between these different pixel types does not simply scale as expected from the difference in total heat capacities described by the small signal energy resolution Eq. (1) ($\Delta E \propto \sqrt{C}$). We attribute this to the very low C of the single-pixel devices resulting in significant nonlinearity in the detector response as a function of energy, which degraded the resolution even at Al-K$_\alpha$, whereas the higher total heat capacity of 4- and 9-pixel hydras resulted in improved linearity and thus energy resolution, when comparing simply
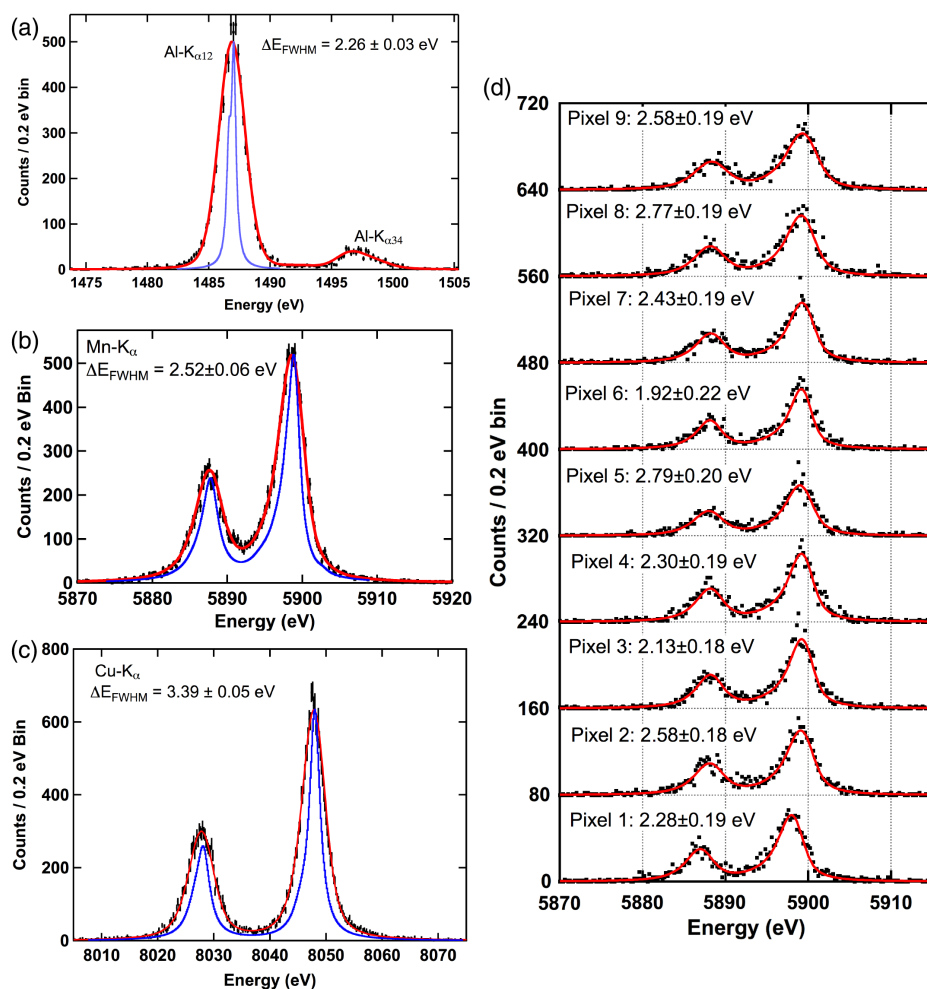
Fig. 5 Co-added spectra for all 9 hydra pixels for (a) Al-Kα (1.5 keV), (b) Mn-Kα (5.9 keV), and (c) Cu-Kα (8 keV) x-rays. The blue line is the natural line shapes derived from Refs. 27–31, and the red line is fit to the data assuming a Gaussian instrument response. (d) The individual pixel spectra for the Mn-Kα measurement. The data for each pixel are vertically offset by 80 counts.

scaling the resolution from the single-pixel result by the $\sqrt{C}$ dependency.

3.3 Identification of Link Hits

From Fig. 4(b), there are clusters of events with rise times in-between the main population of events (indicated by black squares). By examination of the pulse shapes for these events, we believe that they are x-ray absorption events in the Au links that are exposed by the 10-μm gaps between the absorbers. We calculate the Au links will absorb 86% of the incident photons at an energy of 1.5 keV (Al-Kα), which drops to 33% at 5.9 keV (Mn-Kα). The total exposed area of the links is 0.84% of that of the absorbers, thus the total number of events in the links is rel-atively small. Figure 6 (red line) shows the measured average pulse shape for events in the box labeled (a) shown in Fig. 4 (b). These events are thought to be due to hits connecting pixel 1 and pixel 9. Energy deposited in the links will divide between the two absorbers thus the measured rise time has both a fast and a slow component and can be well reproduced by taking the average of the measured events for both pixels (green line). The measured link hit pulse height is 5% less than the predicted average, most likely because of energetic

athermal phonons are lost from the relatively thin links, directly to the substrate, before thermalizing in the film.[32] Though it is important to identify and reject spurious events, the total fraction of these events is small, and we are planning on reducing the absorber gap size to ~4 μm in future design iterations, which would reduce the number of link hits by a factor of 2.5×.

4 Preliminary 20-Pixel Hydra Design and Performance

Here we report on the preliminary results from a single device from a first design iteration that has 20-pixels in a single hydra. This design is a precursor to new devices that will be optimized specifically for the LXM array. With more than about 9 absorb-ers, it becomes less feasible to make a direct thermal link from each absorber to the TES. Thus we have developed a hierarchi-cal structure using trunks and branches that make it easier to design, layout, and achieve uniform spacing of the absorber con-ductances. In this first design iteration, there were five groups of four absorbers, where each group was individually thermally coupled to the TES. Figure 7 shows a schematic layout of the device as well as optical images of 1280 pixels in an 8 × 8 hydra array. Each pixel is on a 50-μm pitch with absorber dimensions of 45 × 45 × 4.2 μm Au and the TES is 25 × 20 μm
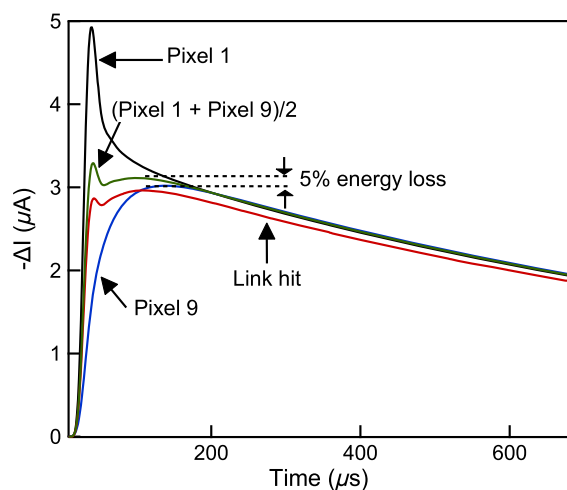
Fig. 6 The red trace shows the average of the events in region "a" indicated in Fig. 4(b). These events are attributed to x-rays that are absorbed directly in the link that connects pixel 1 and pixel 9. When events are absorbed in the links, the energy is split between the two pixels and thus the resulting pulse shape is well-described by the average pulse shape from the two relevant pixels (as illustrated by the green trace). The measured link hits may be smaller than predicted (by ∼5%) because energetic athermal phonons are lost directly to the substrate before thermalizing.

with $T_C \sim 80$ mK. An individual hydra then measures $250 \ \mu m \times 200 \ \mu m$. The position and energy resolution optimization philosophy is essentially the same as for the 9-pixel designs, however, this more complex thermal model adds an additional characteristic pole to the pulse rise- time and thus requires more complex discrimination algorithms than a simple one-pole rise-time estimator (which would result in degenerate position estimation).

Figure 8(a) shows the measured average x-ray pulse shapes for each pixel, which are quite similar to the predicted shapes from the original design [shown in Fig. 8(b)], verifying that the thermal model is a good performance predictor for these complex geometries. These x-rays were produced using a channel-cut crystal monochromator set-up for Cr-K$_{\alpha 1}$ x-rays (5.4 keV),

which has an intrinsic line-width of <0.5 eV.[33,34] In order to determine event position, we used two rise-time metrics to characterize the pre-equilibration signal for every measured x-ray, as opposed to the single rise-time metric used for the standard geometries discussed previously. Figures 8(c) and 8(d) show the rise time determined from the time interval between reaching 5% and 50% of the peak, as a function of that determined from 50% to 90%. To test the wide band spectral and position response, we have carried out measurements using the monochromatic Cr-K$_{\alpha 1}$ (5.4 keV) as well as Mn-K$_{\alpha}$ (6 keV) x-ray photons and in a separate acquisition, we used Al-K$_{\alpha}$ (1.5 keV) and C-K$_{\alpha}$ (277 eV) x-rays. For energies >1.5 keV, the majority of pixels are very well separated using the two rise-time metrics. At 277 eV, there was some position confusion between pixels with the most similar characteristic pulse shapes (rise-time nearest neighbors). For the fastest group, there is some confusion between the 4 pixels even at the higher energies. Our data acquisition system was limited to a maximum sample rate of 2.5 MS/s, with record lengths of 3.3 ms. Because the pulses have very fast ∼1 μs rise times but relatively slow decay times of $\tau_{\text{fall}} = 1.7$ ms, pulse shape measurements were not well sampled over the fast rising edges of the pulses and the pulse shapes were truncated by the short record length (equivalent to ∼2τ_{fall}). The fastest pulses only have ∼4 samples over the leading edge of the pulse to evaluate the rise time, thus the position confusion is likely a result of undersampling combined with nonlinearity of the pulse shape with energy. Alternative position discrimination techniques that use the full pre-equilibration signal to determine position have not been studied for these designs but may ultimately be a better method. Alternatively, adjustments to the thermal link strengths may be required to better separate these pixels.

The measured spectral resolution for the monochromatic Cr-K$_{\alpha 1}$ was very encouraging, achieving $\Delta E_{\text{FWHM}} = 3.38 \pm 0.20$ eV for the RMS of all 20 pixels. Figure 9(a) shows the co-added spectrum for all 20 pixels (totaling ∼65,000 events), which gave a best-fit energy resolution of $\Delta E_{\text{FWHM}} = 3.360 \pm 0.006$ eV, consistent with RMS of the individual pixels. Figure 9(b) shows the histogram of individual resolutions, which ranged 3.06 ± 0.03 eV to 3.73 ± 0.03 eV. These results are already comparable to the preliminary LXM resolution goal
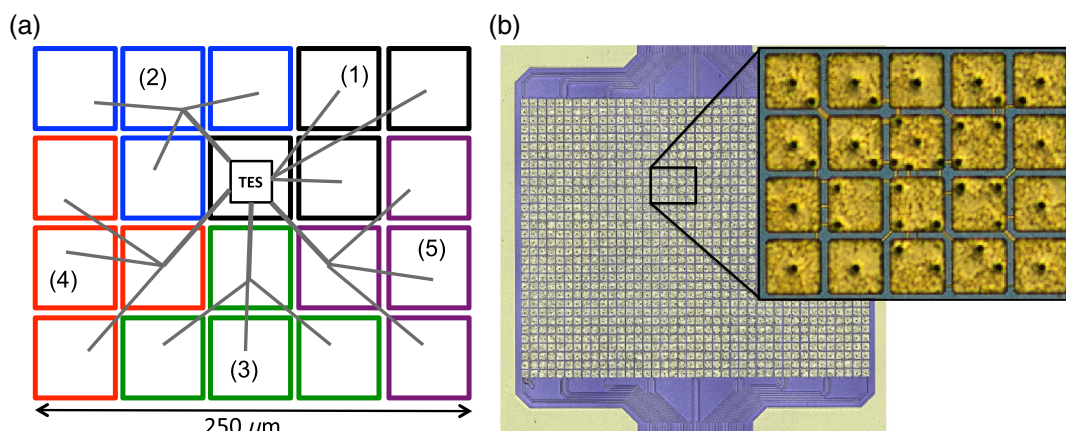

Fig. 7 (a) Schematic of a prototype 20-pixel hydra design showing hierarchical structure of the internal links that connect the pixels to the TES. Each of the 5 groups of 4 pixels is outlined in a different color. (b) Photograph of an 8 × 8 array of 20-pixel hydras (1280 total pixels). The zoom-in shows the 20 pixels of a single hydra.
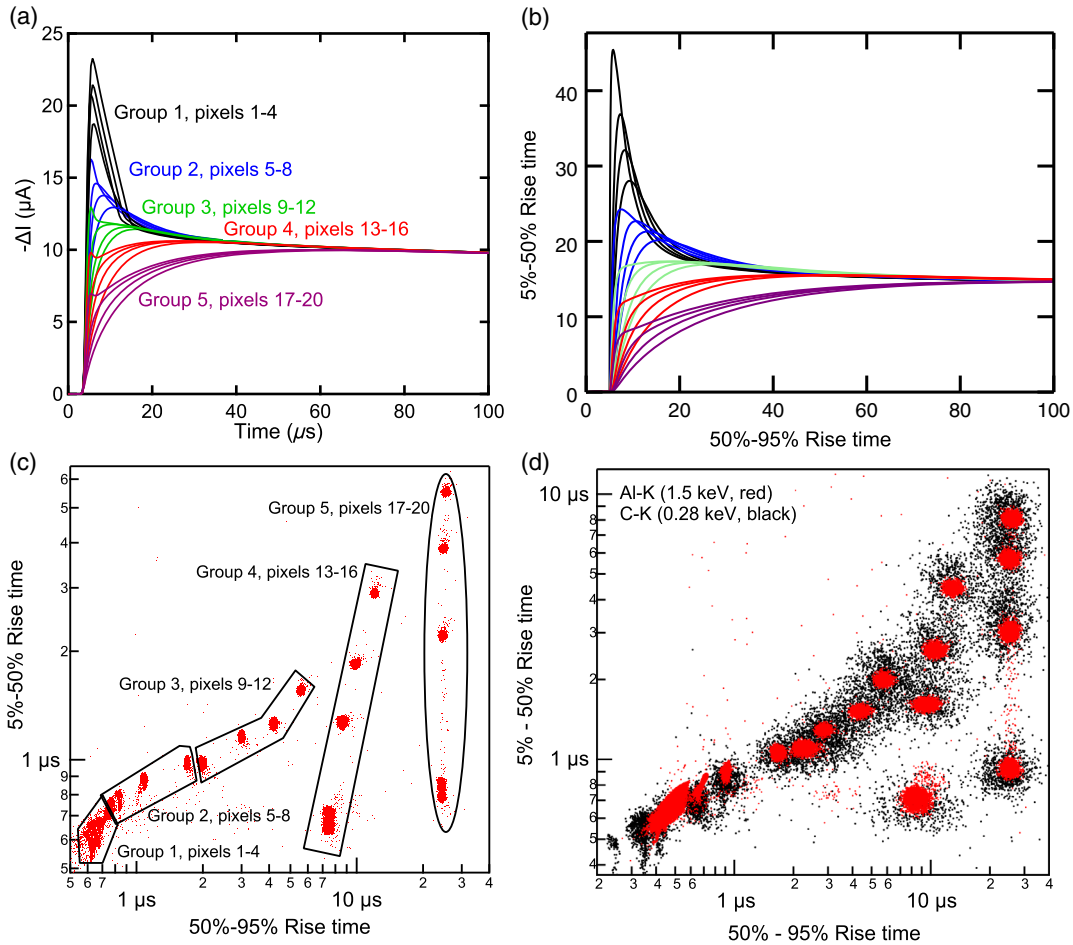
Fig. 8 (a) Measured average pulse shapes for Cr-K$_{\alpha 1}$ x-rays for each of the 20-pixels in the hydra. Each of the 5 groups of 4 pixels is indicated by a different color. (b) The simulated pulse shapes show qualitative agreement with the measurements. (c)A plot of 5% to 50% rise time versus 50% to 90% rise time. X-ray data are included from Cr-K (5.4 keV) and Mn-K (6 keV). The events are separated into distinctive groups as indicated in the caption. All pixels are very well separated except for those in group 1. (d) The same rise-time estimates shown in (c) for a different measurement using Al-K (red dots) and C-K x-rays (black dots). Most pixels are well separated at Al-K, however, nearest neighbor distributions start to overlap at C-K.
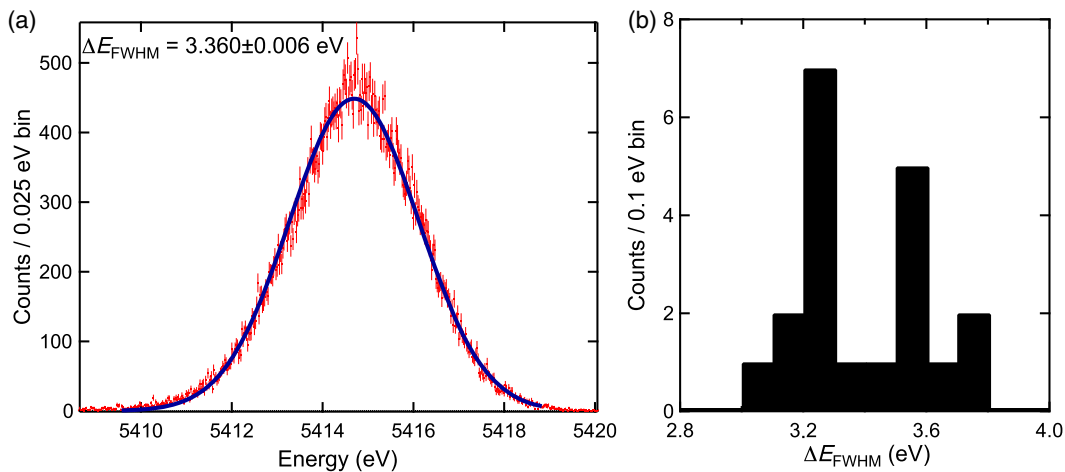

Fig. 9 (a) Co-added spectrum including all 20 pixels in the hydra for monochromatic x-rays taken from Cr-K$_{\alpha 1}$. A Gaussian fit to the energy histogram gives $\Delta E_{\mathrm{FWHM}} = 3.360 \pm 0.006$ eV, consistent with the RMS of individual pixels. (b) Histogram of individual energy resolutions for all 20 pixels.

of ∼3 eV. We estimate that the shorter than typical record lengths used in this experiment may account for ∼0.5 eV degradation in resolution, suggesting that a result below 3 eV could be possible for a fully optimized measurement.

5 Optimization for LXM

We are now focused on optimizing hydras to incorporate 25 pixels per hydra with both 50- and 25-μm absorber designs for LXM. The optimization of any TES design must also take into account constraints imposed by the readout chain (such as noise and bandwidth). The direct readout of large TES microcalorimeter arrays, where each pixel has its own cryogenic (SQUID) and room temperature amplifier chain, is impractical because of the overwhelming burden from the thermal loads on the cooling system as well as the total mass and power requirements this would put on the spacecraft. Thus large format arrays must be read out using a multiplexor. Though a variety of multiplexing schemes are in use for TES readout,[35–37] microwave SQUID multiplexing (μ-Mux)[38] holds the most promise for reading out the large arrays we are developing for LXM. In μ-Mux, each TES signal modulates the frequency of a high-Q microwave resonator. By coupling multiple resonators, each tuned to a unique frequency, to a single GHz bandwidth microwave feedline and cryogenic HEMT amplifier, many 100's of pixels can be read out simultaneously.

TESs are typically operated in or close-to critical damping whereby a large inductance is placed in series with the detector. This is used to reduce the speed of the pixels, which in-turn reduces the bandwidth and dynamic range requirements of the readout. This is usually parameterized by the maximum current slew rate dI/dt, which occurs at the maximum photon energy of interest. In the hydra design, it is the pixel directly thermally coupled to the TES that has the fastest rise time and therefore the largest slew rate. Although some inductance can be used to reduce the slew rate, it is undesirable to critically damp the hydra since this would suppress the high-frequency signal-to-noise ratio required for position discrimination. The maximum slew rate is determined by the initial temperature rise the TES sees. By breaking the hydra down in to more and more pixels, the heat capacity per pixel is decreased and the maximum initial temperature change increases ($\Delta T = E/C$). Thus increasing the number of pixels in a hydra increases the slew rate and makes the readout harder. In order to more optimally match the detector speed to that of the readout, we are exploring design optimizations that also thermally decouple the first pixel from the TES. By removing the fastest pixel in the hydra, the maximum slew rate can be reduced by a factor of a few with only modest loss of energy resolution. Numerical simulation for an optimized 25-pixel hydra with 50-μm pixels and a 4-μm-thick Au absorber (with a total device heat capacity of 0.8 pJ/K and thermal conductance to the bath of 155 pW/K at $T_C = 65$ mK) suggests that we can achieve slew rates of ∼1.5 A/s at 6 keV while achieving an average energy resolution of 3 eV with a decay time constant of 2.5 ms. These designs are currently being fabricated and will be tested in the near future. The successful realization of such a design would enable several hundred hydras to be read out on a single 4-GHz feedline. The μ-Mux and associated room temperature electronics technology development for LXM are discussed in detail elsewhere.[39,40]

6 Summary and Conclusions

We have demonstrated the first results from small pitch hydra designs with 4, 9, and 20 absorbers per TES that are being developed for future x-ray astronomy missions such as Lynx. These results demonstrate the design flexibility to optimize the hydra for a variety of different energy and angular resolution requirements for next generation of x-ray space telescopes. Detailed characterization of a 9-pixel hydra has shown that the thermal properties of the links are well-understood and the x-ray response can be qualitatively well-described by a multibody finite-element model. X-ray measurements in the range 1 to 8 keV have shown that the hydra can achieve excellent broadband energy resolution and imaging capabilities. Significantly, preliminary results on a 20-pixel hydra have demonstrated resolution of 3.4 eV at 5.4 keV, already close to the expected Lynx resolution goal. We have demonstrated the feasibility of distinguishing position over this large number of pixels for a broad range of energies. The position confusion that existed between the fastest pixels is attributed to suboptimal measurement of the rise time and will be studied further on future design iterations. We are now pursuing designs specifically for LXM with 25 pixels per hydra where the slew rates are optimally matched to meet the dynamic range and bandwidth requirements of the proposed readout scheme while maintaining an energy resolution of ∼3 eV.

References

1. K. D. Irwin and G. C. Hilton, "Cryogenic particle detection," in *Topics in Applied Physics*, C. Enss, Ed., Springer, Berlin, Vol. **99**, p. 63 (2005).
2. J. N. Ullom and D. A. Bennett, "Review of superconducting transition-edge sensors for x-ray and gamma-ray spectroscopy," *Supercond. Sci. Technol.* **28**, 084003 (2015).
3. S. J. Smith et al., "Transition-edge sensor pixel parameter design of the microcalorimeter array for the x-ray integral field unit on Athena," *Proc. SPIE* **9905**, 99052H (2016).
4. S. R. Bandler et al., "Development of x-ray microcalorimeter imaging spectrometers for the x-ray surveyor mission concept," *Proc. SPIE* **9905**, 99050Q (2016).
5. D. Barret et al., "The ATHENA x-ray integral field unit (X-IFU)," *Proc. SPIE* **10699**, 106991G (2018).
6. J. A. Gaskin et al., "The Lynx x-ray observatory: concept study overview and status," *Proc. SPIE* **10699**, 106990N (2018).
7. E. Figueroa-Feliciano, "Complex microcalorimeter models and their application to position-sensitive detectors," *J. App. Phys.* **99**, 114513 (2006).
8. R. A. Stern et al., "X-ray microcalorimeter research for solar physics at LMSAL and NIST: an update," *J. Low Temp. Phys.* **151**, 721–726 (2008).
9. F. Mori et al., "Synchrotron beam test of a position-sensitive small-pixel Ir-TES array," *J. Low Temp. Phys.* **151**, 150–154 (2008).
10. S. J. Smith et al., "Characterisation and modelling of transition edge sensor distributed read-out imaging devices," *Nucl. Instrum. Methods Phys. Res. Sect. A* **559**, 500–502 (2006).
11. S. J. Smith et al., "Extended focal plane array development for the international x-ray observatory," *AIP Conf. Proc.* **1185**, 707–710 (2009).
12. S. J. Smith et al., "Development of arrays of position-sensitive microcalorimeters for constellation-X," *Proc. SPIE* **7011**, 701126 (2008).
13. S. J. Smith et al., "Development of position-sensitive transition-edge sensor x-ray detectors," *IEEE Trans. Appl. Supercond.* **19**(3), 451–455 (2009).
14. http://chandra.harvard.edu/.
15. S. J. Smith, C. H. Whitford, and G. W. Fraser, "Optimised filtering for improved energy and position resolution in position-sensitive TES

based x-ray detectors," *Nucl. Instrum. Methods Phys. Res. Sect. A* **556**, 237–245 (2006).

16. S. J. Smith, "Implementation of complex signal processing algorithms for position-sensitive microcalorimeters," *Nucl. Instrum. Methods Phys. Res. Sect. A* **602**(2), 537–544 (2009).

17. J. S. Adams et al., "Real-time data processing for x-ray spectroscopy," *AIP Conf. Proc.* **1185**, 274–277 (2009).

18. S. J. Smith et al., "Optimizing arrays of position sensitive TES's," *J. Low Temp. Phys.* **151**(3–4), 1009–1014 (2008).

19. S. R. Bandler et al., "Advances in small pixel TES-based x-ray micro-calorimeter arrays for solar physics and astrophysics," *IEEE Trans. Appl. Supercond.* **23**, 2100705 (2013).

20. F. M. Finkbeiner et al., "Development of embedded heatsinking layers for compact arrays of x-ray TES microcalorimeters," *IEEE Trans. Appl. Supercond.* **21**(3), 223–226 (2011).

21. S. J. Smith et al., "Small pitch transition-edge sensors with broadband high spectral resolution for solar physics," *J. Low Temp. Phys.* **167**, 168–175 (2012).

22. J. E. Sadleir et al., "Longitudinal proximity effect in superconducting transition-edge sensors," *Phys. Rev. Lett.* **104**(4), 047003 (2010).

23. N. W. Ashcroft and N. D. Mermin, *Solid State Physics*, 1st edn., Saunders College, Philadelphia (1976).

24. F. C. Wellstood, C. Urbina, and J. Clarke, "Hot-electron effects in metals," *Phys. Rev. B* **49**, 5942–5955 (1994).

25. E. T. Swartz and R. O. Pohl, "Thermal boundary resistance," *Rev. Mod. Phys.* **61**, 605–668 (1989).

26. S. J. Lee et al., "Fine pitch transition-edge sensor x-ray microcalorimeters with sub-eV energy resolution at 1.5 keV," *Appl. Phys. Lett.* **107**, 223503 (2015).

27. M. O. Krause and J. H. Oliver, "Natural widths of atomic K and L levels, Kα x-ray lines and several KLL Auger lines," *J. Phys. Chem. Ref. Data* **8**, 329–338 (1979).

28. D. W. Fischer and W. L. Baun, "Diagram and nondiagram lines in K spectra of aluminum and oxygen from metallic and anodized aluminum," *J. Appl. Phys.* **36**, 534–537 (1965).

29. B. Nordfors, "A note on the Al Kα_3 α_4 lines in metal and oxide," *Proc. Phys. Soc. A* **68**, 654–656 (1955).

30. D. A. Wollman et al., "Superconducting transition-edge-microcalorimeter x-ray spectrometer with 2 eV energy resolution at 1.5 keV," *Nucl. Instrum. Methods Phys. Res. Sect. A* **444**, 145–150 (2000).

31. G. Hölzer et al., "K$\alpha_{1,2}$ and K$\beta_{1,3}$ x-ray emission lines of the 3D transition metals," *Phys. Rev. A* **56**, 4554–4568 (1997).

32. A. G. Kozorezov et al., "Athermal energy loss from x-rays deposited in thin superconducting films on solid substrates," *Phys. Rev. B* **87**, 104504 (2013).

33. M. A. Leutenegger et al., "Portable channel-cut crystal monochromators for characterization and calibration of high-resolution x-ray imaging spectrometers," in prep. (2019).

34. M. E. Eckart et al., "Ground calibration of the Astro-H (Hitomi) soft x-ray spectrometer," *J. Astron. Telesc. Instrum. Syst.* **4**(2), 021406 (2018).

35. W. Doriese et al., "Developments in Time-division multiplexing of x-ray transition-edge sensors," *J. Low Temp. Phys.* **184**, 389–395 (2016).

36. H. Akamatsu et al., "TES-based x-ray microcalorimeter performances under AC bias and FDM for Athena," *J. Low Temp. Phys.* **184**, 436–442 (2016).

37. K. Morgan et al., "Code-division-multiplexed readout of large arrays of TES microcalorimeters," *Appl. Phys. Lett.* **109**, 112604 (2016).

38. J. A. B. Mates et al., "Simultaneous readout of 128 x-ray and gamma-ray transition-edge microcalorimeters using microwave SQUID multiplexing," *Appl. Phys. Lett.* **111**, 062601 (2017).

39. D. A. Bennett et al., "Microwave SQUID multiplexing for the Lynx LXM," *J. Astron. Telesc. Instrum. Syst.* **5**(2), 021007 (2019).

40. K. Sakai et al., "Development of space-flight compatible room-temperature electronics for the LXM," *J. Astron. Telesc. Instrum. Syst.* **5**(2) (2019).

Stephen J. Smith received his MPhys degree in physics with space science and technology in 2002 and his PhD in physics in 2006, both from the University of Leicester, UK. He is a University of Maryland Baltimore County (UMBC) associate research scientist, working at NASA's Goddard Space Flight Center. He is an author of more than 100 published papers. His primary research interests are in the development of cryogenic detectors for x-ray astronomy applications.

Simon R. Bandler received his BS degree in mathematical physics from the University of Sussex, UK, and his MS and PhD degrees in physics from Brown University in 1992 and 1996, respectively. He is a research astrophysicist at NASA's Goddard Space Flight Center. He is the author of more than 100 journal papers. His current research interests include transition-edge sensor and magnetic x-ray microcalorimeters, x-ray astrophysics, and the ESA mission called Athena.

Biographies of the other authors are not available.